

## An Analytic Characterization of the Limb Asymmetry - Transit Time Degeneracy

MATTHEW M. MURPHY ,<sup>1</sup> THOMAS G. BEATTY ,<sup>2</sup> AND DANIEL APAI ,<sup>1,3</sup>

<sup>1</sup>Steward Observatory, University of Arizona, Tucson, AZ, 85705, USA

<sup>2</sup>Department of Astronomy, University of Wisconsin–Madison, Madison, WI, 53703, USA

<sup>3</sup>Lunar and Planetary Laboratory, University of Arizona, Tucson, AZ, 85705, USA

### ABSTRACT

Atmospheres are not spatially homogeneous across their entirety. This is particularly true for hot, tidally locked exoplanets which have large day-to-night temperature variation, that yields significant differences between the morning and evening terminators, which is known as limb asymmetry. Current transit observations with the James Webb Space Telescope (JWST) are precise enough to disentangle the separate contributions of these morning and evening limbs to the overall transmission spectrum. However, the signature of limb asymmetry in a transit light curve is highly degenerate with uncertainty in the planet's time of conjunction. As a result, literature measurements of transit times are biased if these planets have significant limb asymmetry, hindering accurate studies of limb asymmetry even with JWST. Although this degeneracy has been discussed in the literature, a general description of it has not been presented.

In this work, we show how the degeneracy between limb asymmetry and the inferred time of conjunction results from apparent changes in the transit contact times when the planetary disk has asymmetric limb sizes. We derive a general analytical formula relating limb asymmetry to the amount that the time of conjunction gets biased, which

*awkward phrasing*

can reach tens of seconds for moderate levels of limb asymmetry. When comparing our formula to simulated observations, we find that numerical fitting techniques add an additional bias to the measured time of conjunction, which results from the different occulting areas of planetary disks of differing size and shape. We also derive an analytical formula for this extra numerical bias, which is on the order of several seconds. These formulae can be applied to planning new observations or interpreting literature measurements, and we show examples for several commonly studied exoplanets.

## 1. INTRODUCTION

Atmospheres are not perfectly uniform in nature. Observational surveys of brown dwarfs and planetary mass objects have found robust evidence that their atmospheres are heterogeneous and variable (e.g., Buenzli et al. 2014; Metchev et al. 2015; Apai et al. 2017). For transiting exoplanets specifically, there is abundant evidence for day-to-night variation in atmospheric temperature and cloudiness (e.g., Beatty et al. 2019; May et al. 2022, among many others) driven by the contrast in irradiation received by the day and night hemispheres. 3D atmospheric circulation models also predict that this day-to-night contrast will drive differences between the morning and evening terminator regions (e.g., Kataria et al. 2016; Line & Parmentier 2016; Powell et al. 2019), which is known as “limb asymmetry” since these terminators form the limbs of the planetary disk seen in transit.

Observational analyses are beginning to confirm these predictions of morning-to-evening limb asymmetry. To date, most measurements of limb asymmetry have come from high-resolution ground-based spectroscopy, which can probe wind speed gradients and single molecule absorption gradients through Doppler shifting (Ehrenreich et al. 2020; Bourrier et al. 2020; Hoeijmakers et al. 2020; Kesseli & Snellen 2021; Borsa et al. 2021). The newly launched James Webb Space Telescope (JWST) has proven capable of directly detecting limb asymmetry at low-resolution as well, which takes the form of apparent time of conjunction variations with wavelength (Feinstein et al. 2022; Rustamkulov et al. 2022) and changes in the spectral transit depth between ingress and egress (Murphy & et al. 2023b, in review; Espinoza & et al. 2023, in preparation; Delisle & et al. 2023, in preparation). Low-resolution

*add a bit  
more description  
of ground-based  
results to flesh  
out P*

*The observational signature of  
limb asymmetry in JWST transit obs. are...*

48 One advantage of the lower spectral resolution data taken w/JWST  
49 observations capture the transmission spectra, both overall and of each limb's contribution, over a  
50 is that it captures... much wider wavelength range than is possible at high resolution, enabling detailed retrievals of the  
51 atmospheric temperature pressure structure, molecular abundances, and aerosol properties in each  
52 spatial region. Extracting these separate contributions is vital to studying and understanding the  
53 circulation of heat and molecules within atmospheres. Also, analyses have shown that if such differ-  
54 ences are ignored, the properties retrieved from observed data can be biased significantly from the  
truth (Feng et al. 2016; Caldas et al. 2019; Taylor et al. 2020).

55 One major obstacle to measuring limb asymmetry via low-resolution transmission spectroscopy is a  
56 degeneracy between the effect of limb asymmetry on the planet's transit light curve and uncertainty  
57 in the planet's time of conjunction. This degeneracy exists because the observable manifestation  
58 of limb asymmetry is a wavelength-dependent difference in the apparent radius of the morning and  
59 evening limbs. Not only does this alter the depth and shape of the light curve during ingress or egress,  
60 but more notably causes the transit to start and end slightly earlier or later. These changes in timing  
61 can be mimicked by varying the planet's time of conjunction, which effectively translates the entire  
62 transit slightly earlier or later in time. For example, models find that extracting limb asymmetry of  
63 approximately a scale height difference in radius requires knowing the time of conjunction to within  
64 less than one second (Line & Parmentier 2016; Espinoza & Jones 2021a). While this degeneracy  
65 has been introduced and its magnitude discussed several times in the literature (e.g. see von Paris  
66 et al. 2016; Line & Parmentier 2016; Espinoza & Jones 2021a; Powell et al. 2019), a generally  
67 applicable analytical description of the degeneracy does not yet exist. In this work, we derive an  
68 analytical description of the degeneracy between limb asymmetry and transit timing, and compare  
69 it to commonly used numerical techniques. We believe this work will be useful for planning and  
70 interpreting observations designed to investigate limb asymmetry.

## 71 2. ANALYTICAL METHOD

### 72 2.1. Defining the problem

*an example**reference fig 1 here*

*observations  
and analyses can't  
bc aware of  
something.*

Consider a planet with asymmetric limbs, where each limb is represented by a semi-circle joined to the other along its flat edge (as in Espinoza & Jones 2021a,b). The evening limb has radius  $R_{evening}$  and the morning limb radius differs by some amount  $\Delta R$ , so that  $R_{morning} = R_{evening} + \Delta R$ . This  $\Delta R$  can be positive or negative depending on which limb is larger, and herein we will assume  $\Delta R$  is positive, so that *this* example planet's morning limb is larger. An observer seeking to study this planet's limb asymmetry must measure both  $R_{evening}$  and  $R_{morning}$ <sup>1</sup> as a function of wavelength, thus constructing separate transmission spectra for each limb. Previous transit observations of this planet, and analyses thereof, were not aware or not capable of measuring limb asymmetry and fit their data assuming the planet has uniform limbs. The planetary radius that these analyses will have inferred is the radius of a uniform circle with the same occulting area – the same transit depth – as the asymmetric-limb disk, which we call the “effective radius”  $R_{eff}$ , calculated as

$$R_{eff} = \sqrt{\frac{1}{2} (R_{evening}^2 + R_{morning}^2)}. \quad (1)$$

Figure 1 shows a schematic of the disk of this asymmetric-limb planet, shown in blue, compared to its uniform-limb equivalent, shown in red, at different points during transit. For reasons described further below, these previous analyses will also have inferred a time of conjunction,  $t_{c,apparent\ uniform}$ , which is offset from the planet's true time of conjunction  $t_{c,true}$  by some amount  $\Delta t_c$  due to the planet's limb asymmetry. In this work, we seek to understand the relationship between  $\Delta R$  and  $\Delta t_c$  and how it depends on the particular planet's properties.

To best intuit the degeneracy between  $\Delta R$  and  $\Delta t_c$ , it is useful to look at the light curve of the asymmetric-limb planet compared to its uniform-limb counterpart. Figure 1 shows an exaggerated example of each at the bottom, which are aligned in time with the sequence of disk schematics at the top. In this example, both planets have the exact same time of conjunction and orbital speed, and are moving from left to right across the stellar disk. The asymmetric-limb planet will begin transit before the uniform-limb planet, because its leading limb, which is  $R_{morning}$ , is larger than

<sup>1</sup> In practice, it is really their corresponding planet-star radius ratios  $R_{evening}/R_\star$  and  $R_{morning}/R_\star$  that are measured from a transit light curve.

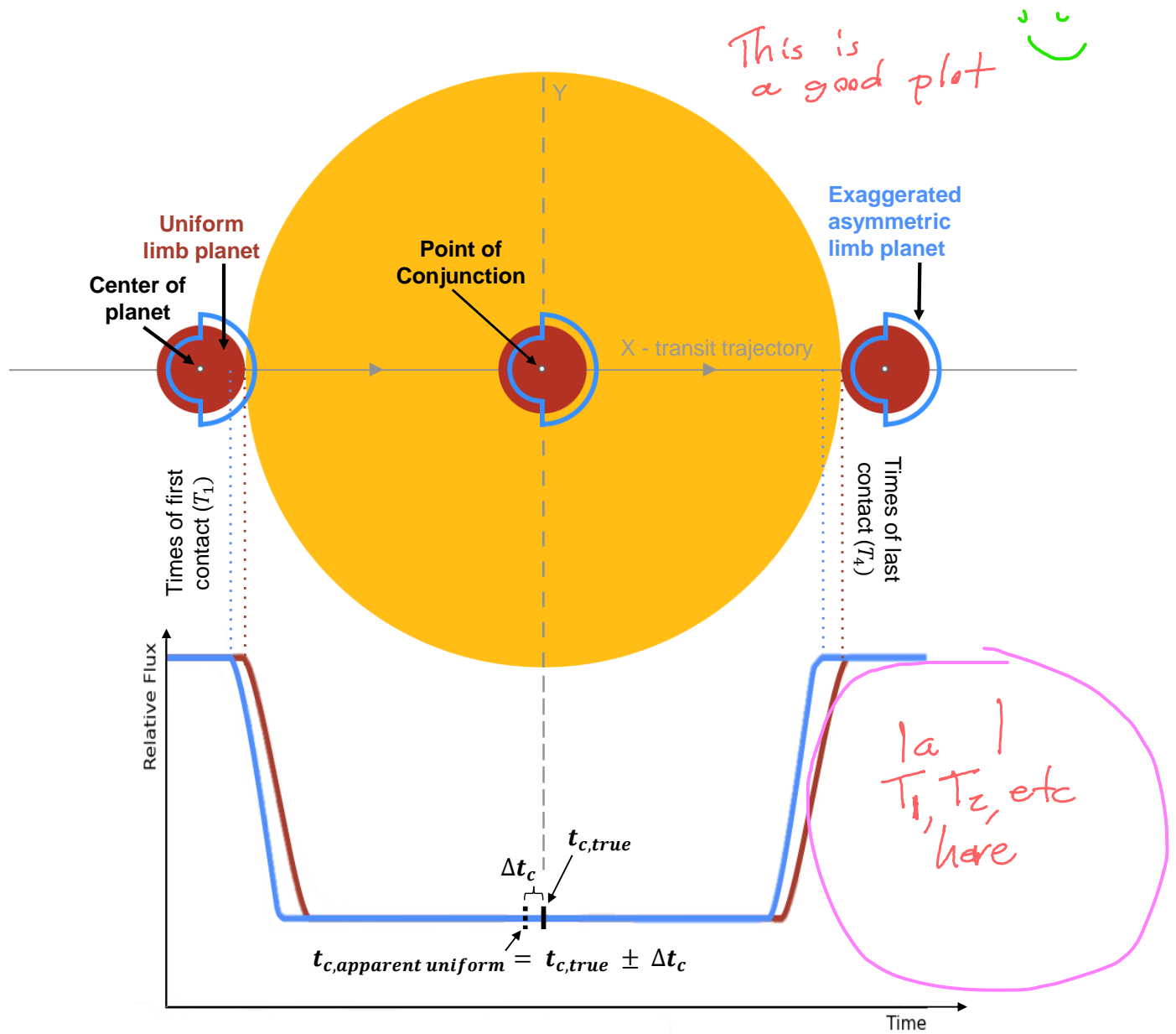


**Figure 1.** Exaggerated schematic illustrating the difference in the transit light curves of an asymmetric-limb planet and a uniform-limb planet. Both planets share the same time of conjunction. Due to the difference in their leading and trailing limb radii though, the transit contact times of each planet differ. An observer that measures the light curve of the asymmetric limb planet, which is shown in blue, and fits their data using a uniform-limb transit model would infer a biased time of conjunction because these changes in the contact times effectively shift the transit earlier or later in time. This is the origin of the degeneracy between limb asymmetry and variations or uncertainty in a planet's time of conjunction.

*the asymmetric-limb*

$R_{eff}$ . Because it has a larger limb, its disk makes first contact ( $T_1$ ) with the stellar disk before the uniform-limb disk does. Similarly, since the asymmetric-limb disks' trailing edge,  $R_{evening}$ , is smaller than  $R_{eff}$ , it is still "ahead" of the trailing edge of the uniform-limb disk so it will also contact the stellar disk first during the end of ingress. The exact same sequence of events occurs during transit  $(T_2)$  ~~for the third ( $T_3$ ) and fourth ( $T_4$ ) contact points,~~ egress. Note that the time at which the disk's trailing edge contacts the stellar disk during ingress is known as "second contact" or  $T_2$ . Similarly, the time at which the leading edge makes contact during egress is "third contact" or  $T_3$ , and that which the trailing edge makes final contact during egress is "fourth contact", "last contact", or  $T_4$ . Since the planets have the same orbital speed, the duration of ~~both~~ each planet's transit is the same. Also note that the shapes of each light curve's ingress and egress is slightly different due to the different shape of each disk, but they reach the same depth during full transit since both disks occult the same total area.

Even though the two planets in Figure 1 have the same ~~true~~ time of conjunction, they have different contact times ( $T_1 - T_4$ ) due to the difference in their limb radii. The net result is an apparent shift in the transit light curve along the time axis. That is, the blue light curve (of the asymmetric-limb planet) in Figure 1 looks like the red light curve (of the uniform-limb planet) but shifted slightly earlier in time. Physically, this corresponds to the uniform-limb planet's apparent time of conjunction  $t_{c,apparent\ uniform}$  being shifted slightly earlier by some amount  $\Delta t_c$ . This is the source of the degeneracy between limb asymmetry and transit timing: the changes in the transit contact times due to limb asymmetry can be effectively mimicked by varying the transit's time of conjunction and keeping the limb radii equal. The consequence for our observer is that the blue light curve is what gets observed in reality, but literature analyses that did not account for potential limb asymmetry would have inferred the planet's time of conjunction to be  $t_{c,apparent\ uniform}$  rather than  $t_{c,true}$ . This presents a problem because even if our observer obtains an ultra-high-precision light curve, if they fix the time of conjunction to  $t_{c,apparent\ uniform}$  in their model, then they will not detect any limb asymmetry as its effect has been effectively canceled out by the systematic error ( $\Delta t_c$ ) in their assumed transit time.

The "fenses" in this para. are for a single planet,  
but the lead sentence refers to both. Make consistent

In the next section, we will derive a description for this degeneracy by solving for the relation between  $\Delta R$  and  $\Delta t_c$ . We take advantage of the fact that, for a circular orbit in the uniform-limb case, the first and last contact times are equidistant from the time of conjunction. As a result, we can transform translations in  $t_c$  to translations in  $T_1$  and  $T_4$  which can be geometrically related to the shape and size of the planetary disk. In essence, we are solving the problem of what  $\Delta t_c$  is necessary to make the  $T_1$  and  $T_4$  of the uniform-limb light curve be the same as those of the asymmetric-limb light curve.

I'd reference one of your figures here, or simplify the description. This is hard to parse

"Two hemispheres next to each other" or something angular momenta vector

### 130 2.2. Times of first and last contact

We assume each planet rotates about a single axis which is oriented parallel to its orbital axis and lies in the plane of the page. The leading and trailing hemispheres, which we again construct as semi-circles, are joined at this rotation axis. The mid-points of the straight edges of each semi-circle are aligned, and a line bisecting the arc of each semi-circle passes through this mid-point and is orthogonal to the rotation axis. Here, we explicitly define the "center" of each planet as the point where this bisector and the rotation axis meet, which is indicated in Figure 1. To aid our derivation, we will work in a cartesian coordinate system as is also shown in Figure 1. The x-axis is aligned along the planet's transit chord, so that the center of the planet is always moving directly along the x-axis. The point of conjunction is the position of the center of the planet at the time of conjunction, defined as when the planet is exactly midway in space (i.e. in  $x$ ) between the points where the center crosses the stellar disk during ingress and during egress. We define this point of conjunction as the origin of our coordinate system, so that the y-axis passes through this point and is orthogonal to the planet's transit trajectory. Note that in Figure 1, we assume the planet transits directly along the stellar equator but this need not be true in general. Our coordinate system is invariant to changes in the planet's orbital alignment as the x-axis can always be translated vertically along the stellar disk and the system rotated such that the x-axis is horizontal.

We assume the planets are of identical mass, which is negligible compared to the mass of the star, and are on identical circular orbits with semi-major axis  $a$  and period  $P$ . The tangential speeds of

This is a good definition, and I think why the previous sentence is so detailed. Reorganize to put this idea first, so readers know why you are going into detail about bisectors etc

149

each planet in their orbit are thus equal and given by

150

$$v_p = \frac{2\pi a}{P}.$$

*multiple  
vs. single  
planet again.(2)*

151

Since these orbits are circular,  $v_x \leq v_p$  since some of the planet's motion is directed in the radial direction except at the point of conjunction. For simplicity, however, we will make the assumption that  $v_x = v_p$  as this correction is generally small enough that it can be neglected.

152

153

When the asymmetric-limb planet makes first contact, assuming it has a larger leading limb, the uniform-limb planet will still need to travel some extra projected distance in the x-direction before it too makes first contact. Let us hold the asymmetric-limb planet fixed at first contact, and let the uniform-limb planet move forward in time until it makes first contact. Then, we solve for the difference in these times via this extra projected distance  $\Delta x$  that the uniform-limb planet travels.

When the planets are transiting along the stellar equator, as is shown in Figure 1, this is simply  $\Delta x = R_{morning} - R_{eff} \approx \Delta R/2$ . However, it is more complicated when the planet's orbit is elevated with respect to the stellar equator, meaning their impact parameter  $b$  is non-zero. In the general case of  $b \neq 0$ , we can use trigonometry to calculate  $\Delta x$ . Figure 2 shows the projected geometry at the point of first contact for an asymmetric-limb planet with non-zero impact parameter. We can draw a triangle whose hypotenuse spans from the center of the stellar disk, through the point of first

contact, to the center of the planetary disk. The length of this hypotenuse is  $R_\star + R_{morning}$  and it makes subtends an angle  $\theta_1$  with respect to the stellar equator. The projected vertical distance between the center of the planet and the stellar equator is  $bR_\star$ , per the definition of the impact parameter. Let us define the position of the center of the asymmetric-limb planet when its leading limb makes first contact as  $x_m$  and likewise for the uniform-limb planet as  $x_u$ . The extra distance travelled by the

uniform-limb planet is

*not  $x_a$   
for asymmetric?*

I was thinking m for morning limb, but that was mostly held-over from a previous conception I had in mind

$$\begin{aligned} \Delta x &= x_m - x_u \\ &= (R_m + R_\star) \cos(\theta_{1,asym.}) \\ &\quad - (R_{eff} + R_\star) \cos(\theta_{1,unif.}). \end{aligned} \tag{3}$$

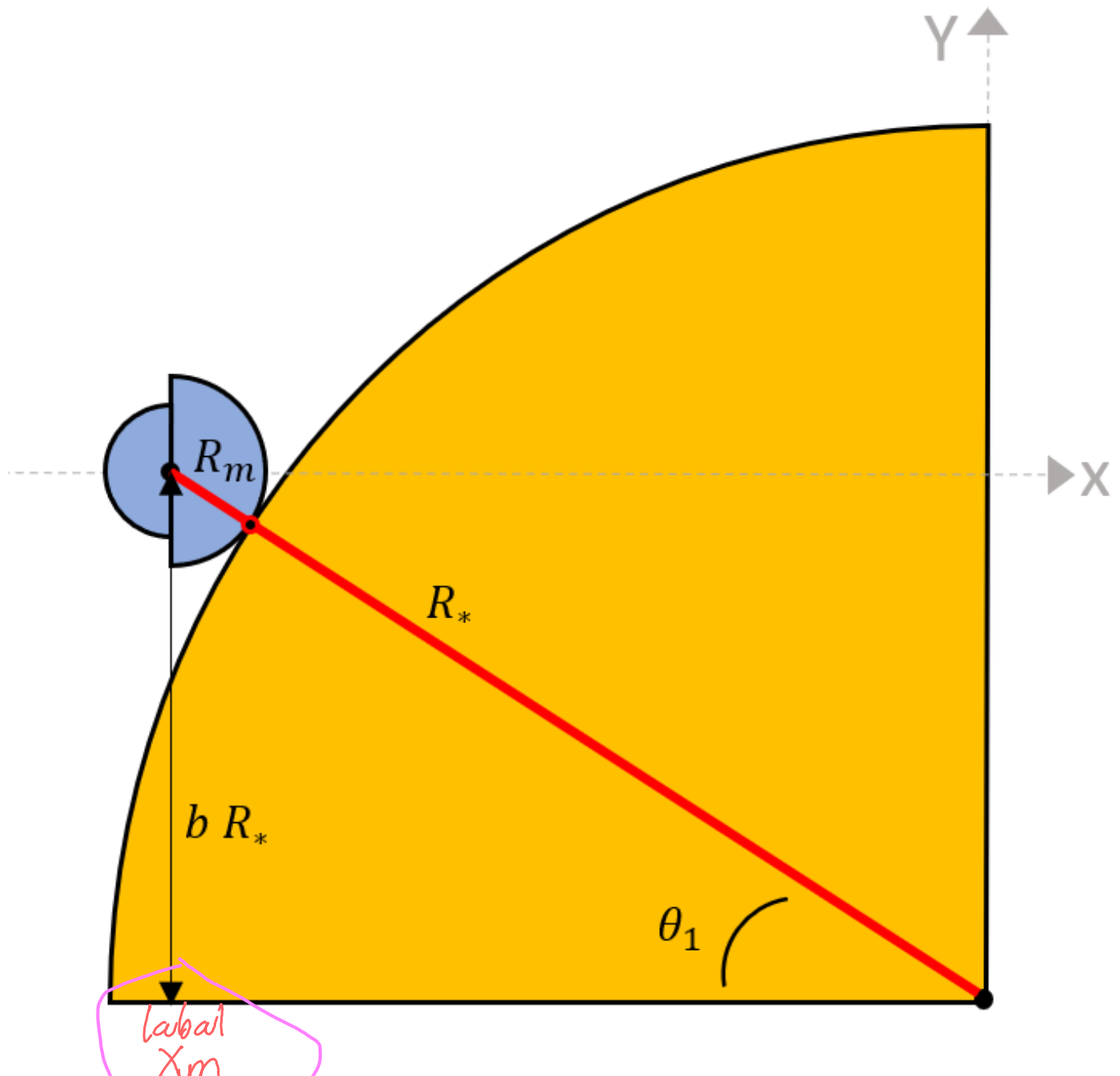


**Figure 2.** Projected geometry of a planet with asymmetric limbs at transit first contact. A line can be drawn from the center of the star to the center of the planet which passes through the point of first contact. This line defines the hypotenuse of a triangle which we use to derive how the exact time of first contact changes as the leading limb radius changes in Equation 9.

*We may also write*

154 Applying the definition of the sine function to the triangle that we constructed in Figure 2, we  
 155 know that

156

$$\sin(\theta_{1,i}) = \frac{bR_\star}{R_\star + R_{p,i}}. \quad (4)$$

157 Here,  $R_{p,i}$  can be  $R_{morning}$  or  $R_{eff}$ . Via trigonometric identities, when  $\sin(x) = y$ ,  $\cos(x) = \sqrt{1 - y^2}$ .  
 158 Therefore,

159

$$\cos(\theta_{1,i}) = \sqrt{1 - \left(\frac{bR_\star}{R_\star + R_{p,i}}\right)^2}, \quad (5)$$

160 and thus

161

$$x_i = (R_\star + R_{p,i}) \sqrt{1 - \left(\frac{bR_\star}{R_\star + R_{p,i}}\right)^2} \quad (6)$$

162

$$= \sqrt{(R_\star + R_{p,i})^2 - (bR_\star)^2}. \quad (7)$$

163 We can then rewrite equation 3 as

164

$$\Delta x = \sqrt{(R_\star + R_m)^2 - (bR_\star)^2} - \sqrt{(R_\star + R_{eff})^2 - (bR_\star)^2}. \quad (8)$$

In the limiting case of  $b = 0$ , this indeed simplifies back to  $\Delta x = R_m - R_u$ . Plugging everything in, assuming  $\Delta T_i = \Delta x/v_p$ , the difference in the times of first contact is then

$$\Delta T_1 = \frac{P}{2\pi a} \left( \sqrt{(R_\star + R_{morning})^2 - (bR_\star)^2} - \sqrt{(R_\star + R_{eff})^2 - (bR_\star)^2} \right). \quad (9)$$

The same derivation can be done for the time of last contact by swapping the morning limb radius for the evening limb radius. In our construction, the uniform-limb planet will also make last contact after the uniform-limb planet, now because the uniform-limb radius is larger than the evening-limb radius. Changing out terms, we then have

$$\Delta T_4 = \frac{P}{2\pi a} \left( \sqrt{(R_\star + R_{eff})^2 - (bR_\star)^2} - \sqrt{(R_\star + R_{evening})^2 - (bR_\star)^2} \right). \quad (10)$$

By construction,  $\Delta T_1$  and  $\Delta T_4$  will always have the same sign. This is because the equivalent-depth uniform radius will always be between the two limb radii, so  $T_1$  and  $T_4$  will always be earlier or later

together. If the asymmetric-limb planet's morning limb is larger than its evening limb, as we have been using in our constructed example, then  $\Delta T_1$  and  $\Delta T_4$  will be negative. If the evening limb is ~~larger~~<sup>larger</sup>, then they will be positive. Then, because these contact times are equidistant about the time of conjunction for the uniform-limb planet,

$$\Delta t_c = \frac{1}{2} (\Delta T_1 + \Delta T_4). \quad (11)$$

### 3. NUMERICAL METHOD

#### 3.1. Setup

To evaluate and compare to our formulae in Section 2.2, we simulated transit observations of the exoplanets WASP-107b, WASP-39b, WASP-96b, and WASP-80b. We chose these specific planets because they span a wide range of bulk atmospheric scale heights, which we use as a measure of the magnitude of limb asymmetry. For these simulations, we collected literature values for several planetary and orbital parameters, which are listed in Table 1. We computed a bulk atmospheric scale height  $H$  of each planet based on the published mass, radius, and equilibrium temperature, and an assumed atmospheric mean molecular weight of 2.3 atomic mass units for each planet. We then followed our previous construction by setting the planet's evening limb radius  $R_{p,evening}$  to the published radius, then compute the morning limb radius as

$$R_{p,morning} = R_{p,evening} + N \times H. \quad (12)$$

Here,  $N$  is any positive number and  $N \times H$  takes the place of  $\Delta R$  so that the radii of the evening and morning limbs differ by some multiple of the planet's bulk scale height.

We then simulated a transit observation of each planet. We first generated a model light curve of the asymmetric-limb planet using the transit modeling package `catwoman` (Jones & Espinoza 2022; Espinoza & Jones 2021b) with literature values for the orbital parameters, the above prescription for the limb radii assuming some value for  $N$ , and assuming the axis separating the limbs is aligned to the orbital axis. We use this model light curve as a reference for generating synthetic observed data, computing the relative flux value of each synthetic data point as as

$$y_{data,i} = y_{model,i} + \mathcal{G}(\mu = 0, \sigma). \quad (13)$$

176 Here, we simulate light curve scatter via the function  $\mathcal{G}(\mu = 0, \sigma)$ , which represents draws from a  
177 Gaussian distribution with a mean of zero and a standard deviation of  $\sigma$ .

178 We first simulated a “perfect” transit observation of the exoplanet WASP-39b in order to best  
179 evaluate our analytical formulae. We placed data points at a cadence of 0.5 seconds and used a light  
180 curve scatter ( $\sigma$ ) of only 1 part-per-million. For this “perfect” observation, we finely sampled  $N$  in  
181 twenty evenly-spaced steps between 0 and 5. Then, we simulated more realistic transit observations  
182 of each planet using the optimal integration cadences computed using `PandExo` (Batalha et al. 2017)  
183 for a JWST/NIRCam F322W2 observation, and light curve scatters of 200 ppm. These computed  
184 cadences are given in Table 1 and ranged from  $\sim$ 15 - 80 seconds between data points. For these  
185 realistic simulations, we used a coarser sampling of  $N$  of ten steps between 0 and 5. For our simulated  
186 observation of WASP-96b only, we found that using its `PandExo` cadence of 144 s and this 200 ppm  
187 scatter led to very large noise in the result which made comparing its results to the other planets’  
188 difficult and non-instructive. Therefore, the results for WASP-96b we present herein instead use a  
189 cadence that is twice as frequent (72 s) and a light curve scatter of 150 ppm. As we will discuss  
190 further in Section 3.5, using these different parameters for WASP-96b did not change the underlying  
191 result, but only made it easier to present visually by reducing the scatter about this underlying  
192 result. The magnitudes of light curve scatter were chosen arbitrarily so that it would be (otherwise)  
193 uniform between planets, precise enough to enable a good fit, and be achievable with a real JWST  
194 observation. In all cases, we assumed having an equal time out-of-transit baseline to the published  
195 transit duration.

196 After generating the simulated observed data, we fit these data using a uniform-limb transit model  
197 generated by the transit modelling package `batman` (Kreidberg 2015). We left all parameters fixed  
198 to their true values except for the time of conjunction, which was allowed to vary freely. We set  
199 the planetary radius to the value which would have the same planetary disk occulting area as the  
200 corresponding asymmetric-limb disk, using equation 1. We fit the data using the Markov Chain Monte  
201 Carlo method using `emcee` (Foreman-Mackey et al. 2013), sampling just the time of conjunction for  
202 5,500 steps which was more than sufficient for each run’s sampling to converge.

203 We chose to use uniform limb darkening when generating the reference light curves, meaning the  
204 stellar disks are completely uniform in brightness. This choice was partially motivated by computa-  
205 tional efficiency, as the overhead initializations of `catwoman` and `batman` are significantly slower when  
206 limb darkening must be computed. It was also motivated by our desire to treat each planet uniformly,  
207 as different host stars exhibit different limb darkening that may yield different results depending on  
208 the assumed cadence or noise of the light curve. We did test various limb darkening laws, including  
209 quadratic and logarithmic, and various sets of limb darkening coefficients. We found that the precise  
210 choice of limb darkening did not change our result because we set the limb darkening when generating  
211 the reference light curve and kept it fixed for all later steps, thus assuming perfect knowledge of limb  
212 darkening during the light curve fitting. Uncertainty in the limb darkening coefficients is of concern  
213 to real observations, but is beyond the scope of our analysis and can be mitigated using stellar models  
214 in practice.

### 215           3.2. *Connection to literature measurements*

216 Our numerical method described in Section 3.1 resembles the method by which most, if not all,  
217 literature measurements of exoplanet transit times are determined. In reality, one obtains a transit  
218 observation of an exoplanet which may or may not have asymmetric limbs. The data is then typically  
219 fit using a uniform-limb model, using `batman` or similar light curve models, typically using a Bayesian  
220 parameter sampling technique, such as `emcee`. Therefore, using this numerical method we are able  
221 to directly compare our analytical predictions to what one may measure from a real observation,  
222 and thus evaluate any inconsistencies between them which would have implications for literature  
223 measurements.

### 224           3.3. *Verifying our analytical derivations*

225 First, we recorded the reference light curves generated for the “perfect” observation, determined  
226 the first ( $T_1$ ) and last ( $T_4$ ) contact times of each light curve, and calculated the change in both  
227 relative to the  $N = 0$  (i.e. uniform-limb) case as  $N$  increased. We compared these changes to what  
228 Equations 9 and 10 predict, which is shown in Figure 3. We find that our formulae perfectly predict

**Table 1.** Planetary and Stellar Properties used in our Transit Observation Simulations.

Parameter [units]	WASP-80 b	WASP-96 b	WASP-39 b	WASP-107 b
P [days]	3.06785271(19) <sup>a</sup>	3.4252565(8) <sup>a</sup>	4.0552941(34) <sup>f</sup>	5.721488(3) <sup>a</sup>
a / R <sub>s</sub>	12.63 ± 0.13 <sup>b</sup>	9.03 ± 0.30 <sup>d</sup>	11.55 ± 0.13 <sup>g</sup>	18.2 ± 0.1 <sup>j</sup>
i [degrees]	89.02 ± 0.11 <sup>a</sup>	85.6 ± 0.2 <sup>c</sup>	87.32 ± 0.17 <sup>f</sup>	89.7 ± 0.2 <sup>j</sup>
R <sub>p</sub> / R <sub>★</sub>	0.17137(39) <sup>a</sup>	0.1186(17) <sup>d</sup>	0.1457(15) <sup>h</sup>	0.14434(18) <sup>k</sup>
R <sub>★</sub> [R <sub>⊙</sub> ]	0.605 ± 0.048 <sup>*</sup>	1.15 ± 0.03 <sup>*</sup>	0.92 ± 0.03 <sup>*</sup>	0.73 ± 0.15 <sup>*</sup>
M <sub>p</sub> [M <sub>Jupiter</sub> ]	0.538 ± 0.035 <sup>a</sup>	0.49 ± 0.04 <sup>e</sup>	0.281 ± 0.032 <sup>f</sup>	0.096 ± 0.005 <sup>l</sup>
T <sub>eq</sub> [K]	825 ± 19 <sup>a</sup>	1285 ± 40 <sup>c</sup>	1166 ± 14 <sup>f</sup>	770 ± 60 <sup>j</sup>
T <sub>14</sub> [hours]	2.131 ± 0.003 <sup>a</sup>	2.4264 ± 0.0264 <sup>c</sup>	2.8032 ± 0.0192 <sup>i</sup>	2.753 ± 0.007 <sup>j</sup>
μ [amu]	2.3	2.3	2.3	2.3
H [km]	226 ± 44	669 ± 97	1042 ± 171	1221 ± 174
Cadence [s]	14.8	72.0	79.5	20.2
σ [ppm]	200	150	200	200

**References**—a-Kokori et al. (2022), b-Triaud et al. (2015), c-Hellier et al. (2014), d-Patel & Espinoza (2022), e-Bonomo et al. (2017), f-Mancini et al. (2018), g-Fischer et al. (2016), h-Maciejewski et al. (2016), i-Faedi et al. (2011), j-Anderson et al. (2017), k-Dai & Winn (2017), l-Piaulet et al. (2021), \*-Gaia Collaboration et al. (2018)

**NOTE**— Uncertainties with many digits are given in parenthetical form, where the values of N digits in each parenthesis replace the last N significant digits of the measured value. For example, 0.03(1) means 0.03 ± 0.01. Values without associated references were either assumed or calculated based on other values.

Parameter definitions:  $P$  = orbital period,  $a$  = semi-major axis,  $R_*$  = stellar radius,  $i$  = orbital inclination,  $R_p$  = planetary radius,  $M_p$  = planetary mass,  $T_{eq}$  = planetary equilibrium temperature,  $T_{14}$  = transit duration,  $\mu$  = bulk mean molecular weight,  $H$  = bulk atmospheric scale height, Cadence = synthetic observation data cadence,  $\sigma$  = synthetic observation light curve scatter.

the changes in the model light curves'  $T_1$  and  $T_4$ . In terms of magnitude, we find that  $T_1$  occurs over 40 seconds earlier when the morning limb radius is increased by 5 scale heights. Note that the time of last contact does not change because it depends on changes in the evening limb radius which we kept fixed. Also, we remind the reader that these light curves were generated using WASP-39b's

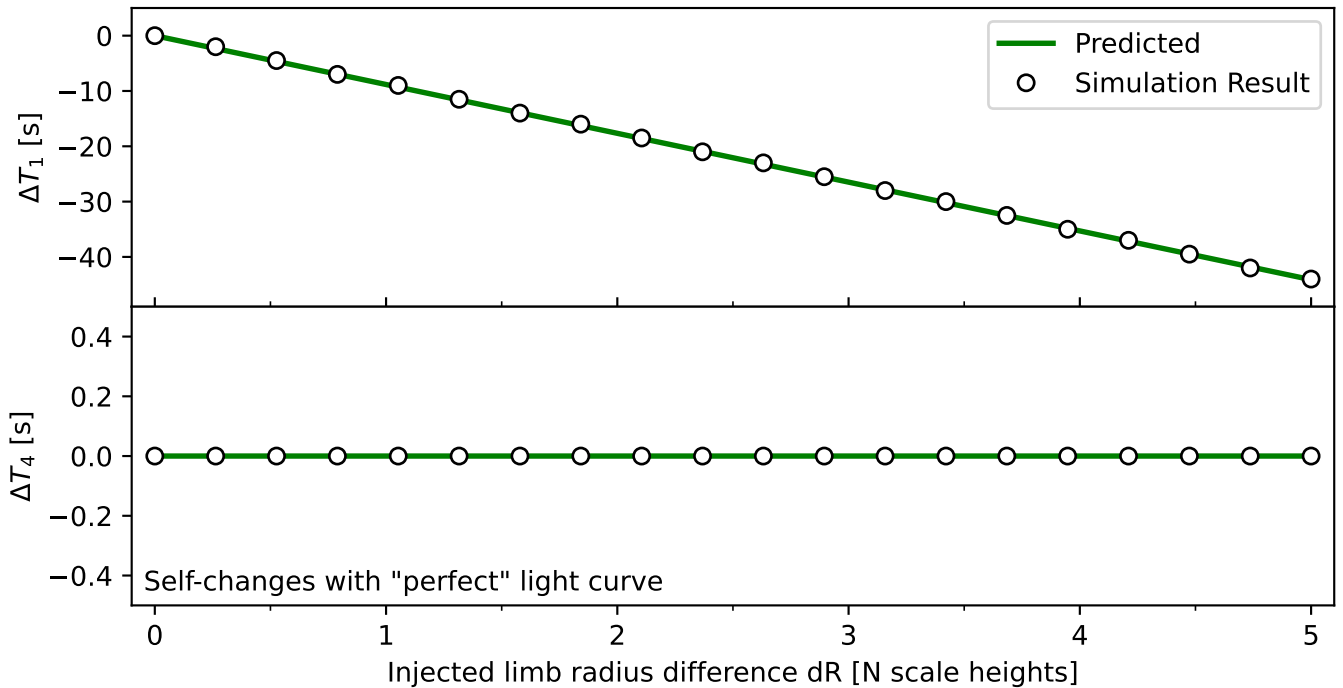


**Figure 3.** Changes in the time of first ( $\Delta T_1$ ) and last ( $\Delta T_4$ ) contact due to extending the radius of our example planet’s morning limb relative to the evening limb. We defined this radius extension  $dR$  in multiples of the planet’s atmospheric scale height, as given on the x-axis. For this example, we used literature parameters for the planet WASP-39b and generated light curves using the transit model `catwoman` for each  $dR$ . Then, we recorded how  $T_1$  and  $T_4$  of each light curve changed relative to the case of uniform limb sizes (i.e.  $dR = 0$ ), shown as the black points. We compare these results to our analytical predictions for  $\Delta T_1$  and  $\Delta T_4$ , given in Equations 9 and 10, which we find perfectly predict the numerical results.

orbital parameters which is an inclined orbit, thus verifying that Equations 9 and 10 indeed handle general orbits well.

Then, we compared the best-fit time of conjunction of the uniform-limb model on the “perfect” observation’s simulated data to the true value, which is  $\Delta t_c$ , shown as the points in Figure 4. We compared this numerical result to our analytical prediction for  $\Delta t_c$  from Equation 11, shown as the blue line. We find that our simulated fit finds a larger  $\Delta t_c$  than is predicted by a factor of about 10% at all  $N$ . The discrepancy between our numerical result and analytic prediction reaches nearly three seconds at our maximal case of limb asymmetry of  $N = 5$ . Through trial and error, we found that this discrepancy is a general result for any choice of planet or light curve parameters we used,

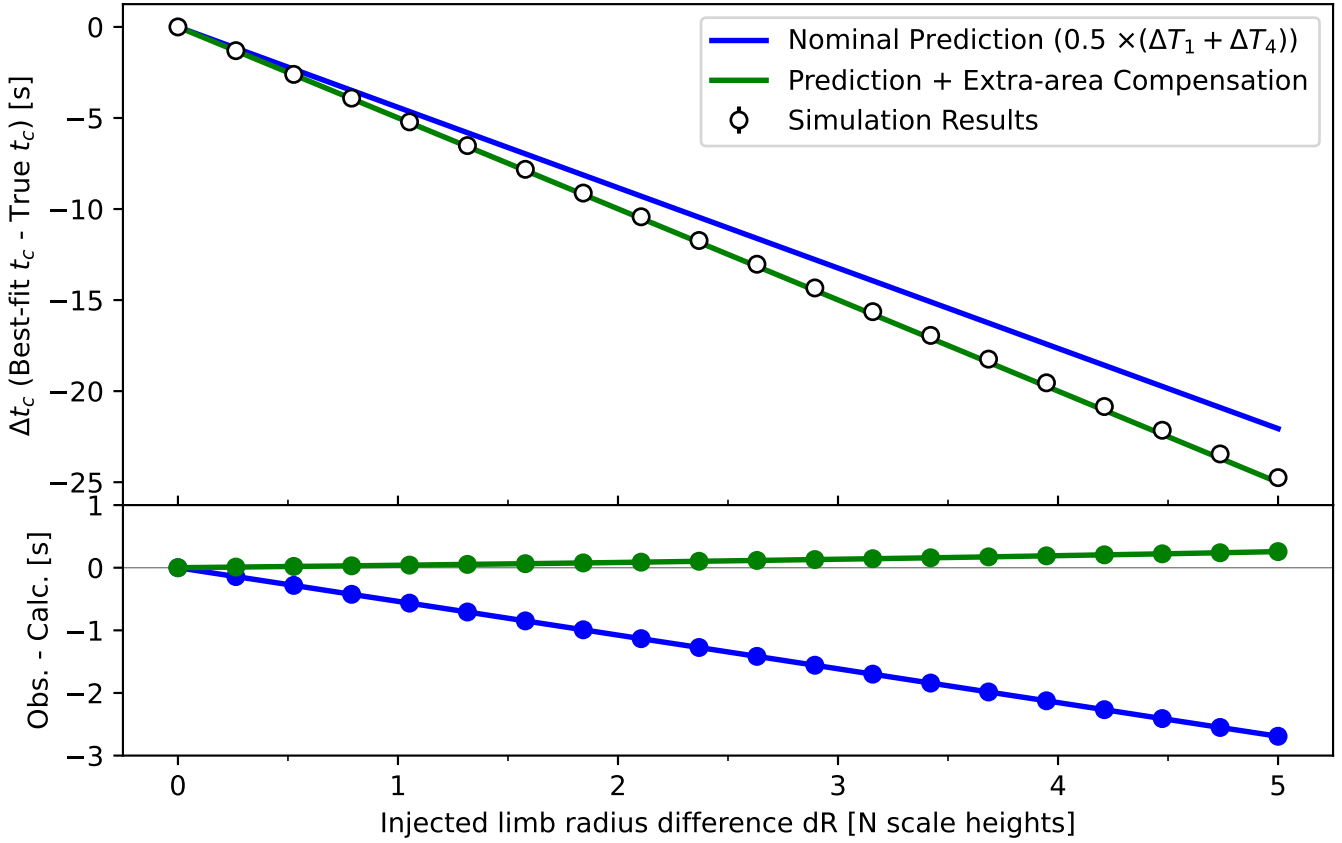


**Figure 4.** Measured times of conjunction compared to the true times of conjunction, as a function of the injected difference in radius between the planet’s evening and morning limbs. The points show our numerical results obtained from fitting a synthetic observation of WASP-39b with ideal cadence and light curve scatter, where the data is generated around an asymmetric-limb transit model but fit using a uniform-limb transit model. The blue line shows our analytical prediction for this bias in  $t_c$  from Equation 11, derived from the extra distance that a uniform-limb disk with the originally same  $t_c$  as an asymmetric-limb disk needs to travel before they have the same first and last transit contact times. We find a discrepancy between this analytical prediction (in blue) and the result of our simulated observations (black points) which is due to the numerical extra-area compensation effect, described in Section 3.4. The green line includes this compensation effect, derived in Equation 18, which we see brings the analytical and numerical results into agreement.

leading us to discover that there is an underlying physical mechanism which we explain in the next section.

### 3.4. Extra-area compensation when fitting transits

The discrepancy between our numerical simulation result and our analytical prediction, as shown in Figure 4, stems from an inherent difference in what each aims to measure. Our analytical formula was derived to specifically calculate the  $\Delta t_c$  required to make the  $T_1$  of the asymmetric-limb and uniform-limb planets match. In the numerical method, we are instead calculating the “best-fit”  $t_c$  of the uniform-limb model when it is applied to the data generated from an asymmetric-limb model. The “best-fit” solution is determined not strictly by making the  $T_1$  values match, but by whatever value of the parameter optimizes the goodness-of-fit metric used by the fitting routine. In our case, this metric was the Bayesian likelihood. We find that our discrepancy results from an overcompensation in  $\Delta t_c$  by the numerical sampling which, due to the geometry of the planetary disks, better minimizes the residuals between the light curves of the data (i.e. the asymmetric-limb model) and the uniform-limb model compared to the analytical solution. This is a purely numerical effect which we dub the “extra-area compensation effect”, for reasons we outline below.

We illustrate how this extra-area compensation effect arises in Figure 5. The planetary disks represented by our model light curves are shown for reference in panel A, with the uniform-limb planet’s disk in red and the asymmetric-limb planet’s disk in blue. Panels B, C, and D represent the planet approaching transit, with the star represented as the uniform yellow-orange disk. We start by treating the planets as having the same  $t_c$ , shown in panel B. In panel C, we proceed to the time when the asymmetric-limb planet makes first contact with the stellar disk. Nominally, when the two planets have the same  $t_c$ , the uniform-limb planet would not yet be making first contact but would take some extra time  $\Delta t_c$  before it does. Our analytic formula solves for  $\Delta t_c$  so as to make both planets make first contact at exactly the same time, as is illustrated in panel C. In this arrangement, however, the asymmetric-limb planet has two regions of extra occulting area due to its larger leading limb which are indicated by the blue arrows. During the first half of transit ingress, these regions of extra occulting area will lead to the asymmetric-limb planet having larger transit depth and a steeper ingress slope, thus causing a large residual between the two planets’ light curves despite them making first contact at the exact same time. The numerical approach disfavors this arrangement as a solution due to this large residual, hence it finds a different solution. As we see from the residuals

with the blue line in Figure 4, the numerical approach prefers an even larger  $\Delta t_c$  which is equivalent to moving the uniform-limb planet even further to the right in our schematic. This favored numerical solution is illustrated in panel D, where the uniform-limb planet now has  $\Delta t_c + \tau$ , where  $\tau$  represents the extra timing bias compensated by the numerical approach. This arrangement is preferred by the numerical approach because, as a result of the uniform-limb planet now being slightly ahead of the asymmetric-limb planet, the uniform-limb planet now has some extra occulting area at the leading edge of its disk as indicated by the red arrow. This red-arrow area effectively cancels out the blue-arrow areas, and an equivalent effect happens with the trailing disk edges. As a result, neither disk has net excess occulting area, leading to a minimized residual between their light curves during ingress and egress.

We derive an analytical formula for this extra-area compensation  $\tau$  by considering the extra path length required to be traveled by a planet with increased hemisphere radius during ingress before that hemisphere becomes fully internally tangent. Figure 6 sketches this situation, where we have aligned the uniform-limb and asymmetric-limb disks from our schematic in Figure 5 such that they are concentric (i.e. share the same  $t_c$ ) and are positioned where the center of the planet contacts the stellar disk. Note that we have folded the asymmetric-limb planet so that both of its hemispheres are entering transit for illustration purposes. Each planet's motion is purely upward along the y-axis as time progresses<sup>2</sup>. At this point in time, each planet still has extra area in the bottom right which is yet to occult the star. Therefore, each disk must still travel a certain distance until its polar point – the edge of the disk on the x-axis – also contacts the stellar disk edge at which point the shown hemisphere would become fully internally tangent. This length is equal to a line drawn from the polar point to the the edge of the stellar disk, represented as the thick black curve, at the same  $x$ . We show an example for the asymmetric-limb planet's larger morning hemisphere as the orange points and orange connecting line. In the coordinate system shown in Figure 6, the length of this line is just equal to the y-value of the curve defining the stellar disk edge as a function of x. The

<sup>2</sup> In this derivation, the meaning of the x- and y-axes are flipped relative to what we used in Figures 1 and 2

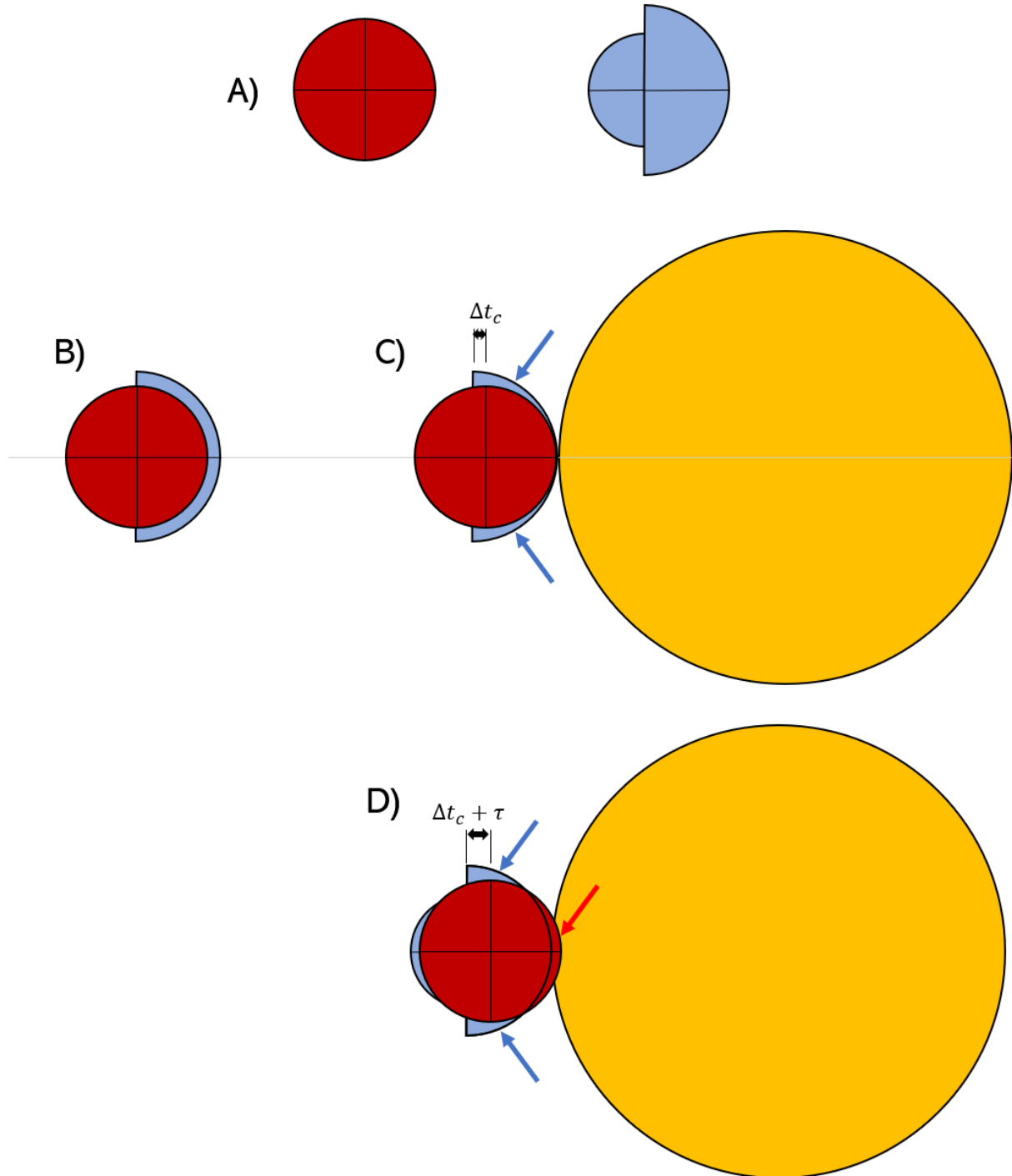


**Figure 5.** Schematic of the extra-area compensation problem. Panel A shows the uniform-limb disk in red, which is used in the model being fit to the synthetic data generated based on the asymmetric-limb disk, which is shown in blue. These two model planets are initially set to have the same time of conjunction  $t_c$ , in which case their disks are overlaid as in Panel B. Due to limb asymmetry imprinted into the data, this fit will return a biased  $t_c$  when using this uniform-limb model. Panel C shows our analytic solution for how much this bias ( $\Delta t_c$ ) will be, derived from the extra distance that the uniform-limb disk needs to travel along the transit trajectory until its first (and last) contact times are the same as for the asymmetric-limb disk. The extra occulting area of the asymmetric-limb disk in this arrangement, indicated by the blue arrows, leads to a large fitting residual and thus is disfavored by our numerical fit. Rather, the numerical fit prefers

stellar disk is a uniform circle of radius  $R_\star$  and is centered at  $x=0$ ,  $y=R_\star$  in these coordinates, so its disk edge is defined by

$$x^2 + (y - R_\star)^2 = R_\star^2, \quad (14)$$

which can be solved for  $y$  to give

$$y = R_\star - \sqrt{R_\star^2 - x^2}. \quad (15)$$

Note that  $x$  and  $y$  are both distances in this equation. This full  $y$ -length is not needed, however. By the time the planet has traversed approximately  $y/2$ , an equal area to what remains below the curve will have appeared above the curve. This represents the condition of achieving the mutually canceling occultation areas that we illustrated in panel D of Figure 5, and is what defines the magnitude of the resulting over-compensation. This compensation  $\tau$  is then related to the difference in  $y/2$  between the uniform-limb and asymmetric-limb planet, which via equation 15 depends on the difference of their limb radii and the (fixed) radius of the star. To convert this difference in path length to a duration of time, we simply divide by the (fixed) orbital speed. The result is

$$\tau = \frac{\Delta y}{2v_p} \quad (16)$$

$$= \frac{1}{2v_p} \left[ \left( R_\star - \sqrt{R_\star^2 - x_1^2} \right) - \left( R_\star - \sqrt{R_\star^2 - x_2^2} \right) \right] \quad (17)$$

$$= \frac{1}{2v_p} \left[ \sqrt{R_\star^2 - x_2^2} - \sqrt{R_\star^2 - x_1^2} \right] \quad (18)$$

Here,  $x_1$  and  $x_2$  represent the polar radii of the larger and smaller hemispheres, respectively. In our case, these are the radii of the asymmetric-limb planet's morning limb and the uniform-limb planet. Therefore, we would have

$$\tau = \frac{1}{2v_p} \left[ \sqrt{R_\star^2 - R_{eff}^2} - \sqrt{R_\star^2 - R_{morning}^2} \right]. \quad (19)$$

We compute the expected extra-area compensation for our “perfect” observation of WASP-39b scenario using equation 19 and add it to our nominal prediction from equation 11. The result is shown as the green line in Figure 4, which we see ends up matching the numerical result. This validates that our derived compensation  $\tau$  is indeed the cause of the difference between our nominal analytic formula and our numerical results. There is still outstanding residual between these combined

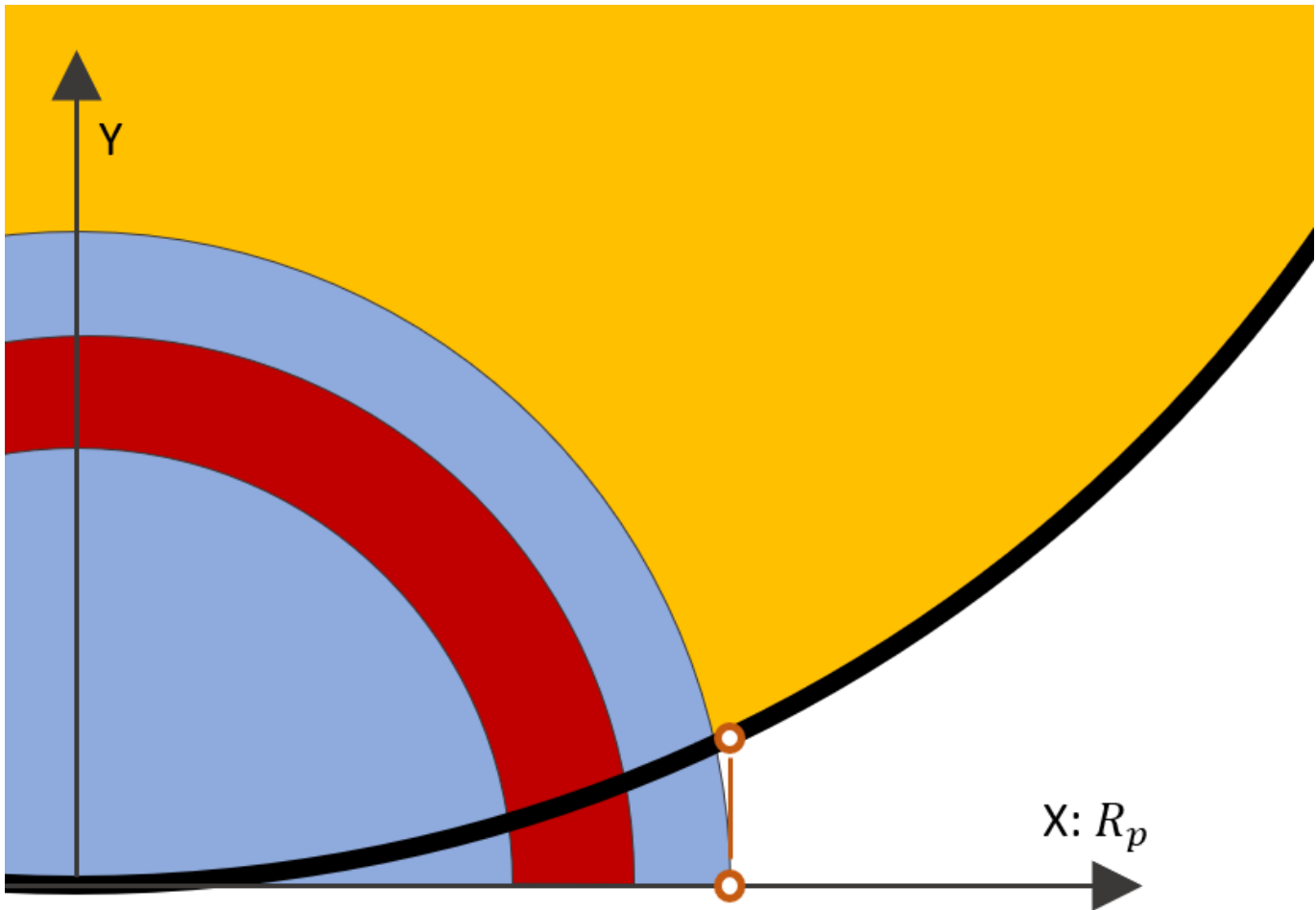


**Figure 6.** Schematic showing the extra distance necessary for a disk hemisphere to travel between the point when the whole-disk center is contacting the disk and the point when the entire hemisphere will be internally tangent. The blue and red semi-circles represent the hemispheres of our uniform-limb and asymmetric-limb planets shown in Figures 1 and 6, and the orange circle is the star. This extra distance is equal to the y-value of the stellar disk at a given x, where the x-coordinate is described by the radius of the disk hemisphere. We use this as the basis for our derivation of the extra-area compensation given by Equation 18.

298 formulae and our numerical result, but it is only a tiny fraction of a second up to N=5 which is  
 299 a significant improvement over the several seconds of residual when not accounting for extra-area  
 300 compensation.

301

### 3.5. “Realistic” case results

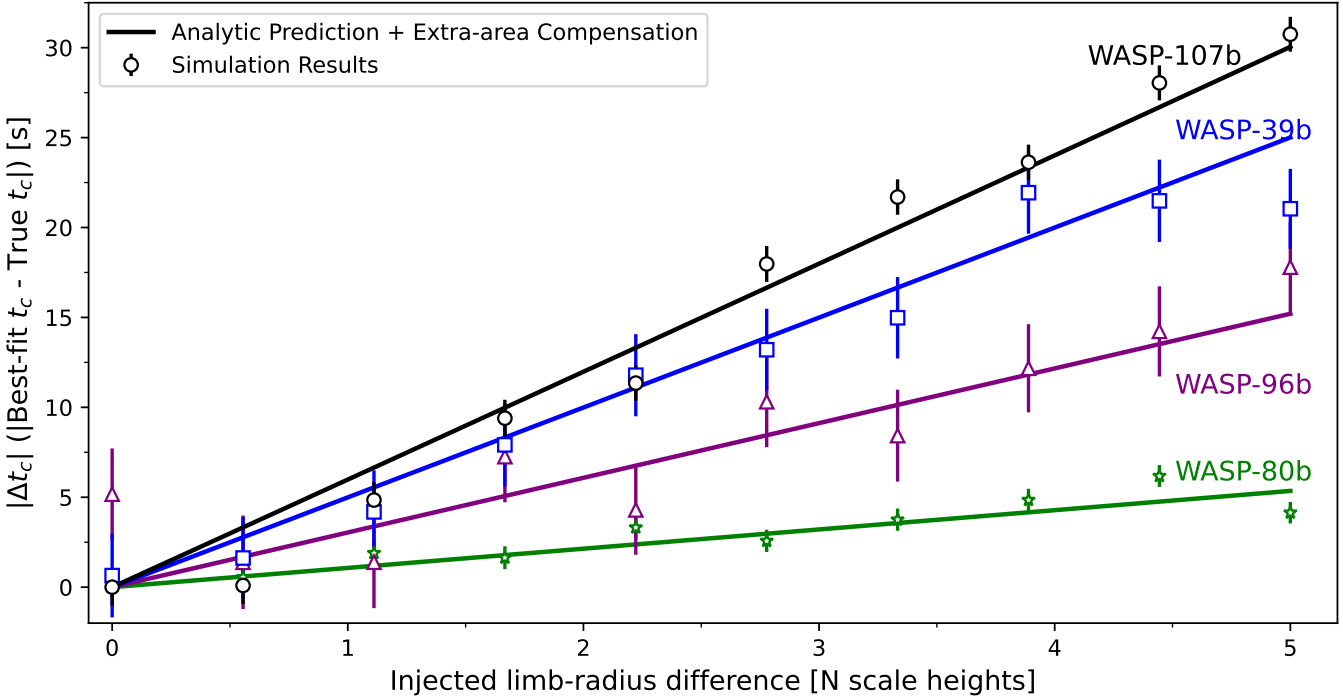


**Figure 7.** Measured times of conjunction compared to the true times of conjunction ( $\Delta t_c$ ) as a function of the injected limb radius difference for simulated observations of several representative exoplanets. For each observation, we simulated data based on an asymmetric-limb transit model but fit them using a uniform-limb transit model, similar to what may happen with real observations. The solid lines represent our analytical predictions for  $\Delta t_c$  as calculated using Equation 11 and including the numerical extra-area compensation effect described by Equation 18. We find that our analytical prediction, when accounting for this numerical overcompensation, matches our simulated observation results. The outstanding residuals are due purely to the injected light curve scatter and coarse cadence used for the simulated data. Our equations therefore describe how a time of conjunction measured from a transit observation is biased if the planet has limb asymmetry but is fit assuming uniform-limbs, enabling this bias to be evaluated in literature measurements as well as predicted for future observations.

Now we return to the results of our “realistic” simulated observations of WASP-80b, WASP-96b, WASP-39b, and WASP-107b described in Section 3.1. We plot the best-fit timing biases  $\Delta t_c$  as a function of  $N$  for each simulation in Figure 7. We compare these to the corresponding analytical prediction for each planet from Equation 11, with the corresponding compensation bias from Equation 18 accounted for by adding it to this prediction. We see that our numerical results agree

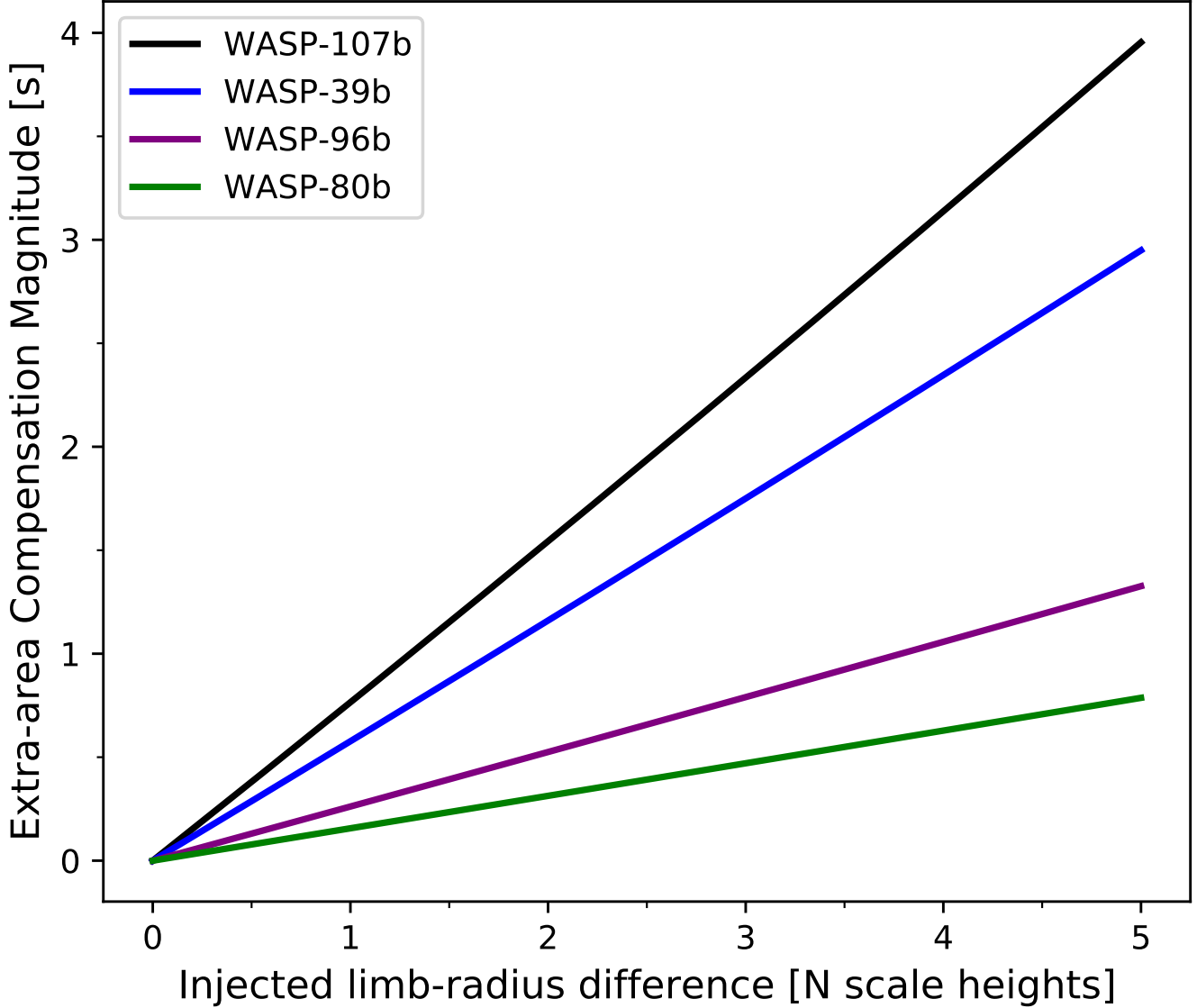
extremely well with our analytical predictions when accounting for the extra-area compensation. The remaining residuals are solely a result of the noise and cadence of each simulated observation.

Figure 8 shows the calculated magnitude of the numerical extra-area compensation corrections for each planet. We find that the correction at any given  $N$  is larger for planets with larger atmospheric scale heights, like WASP-39b and WASP-107b. That is, this numerical overcompensation is larger when modeling a planet with a larger difference in physical radius between its limbs. Even for our most extreme case of WASP-107b, however, this magnitude of this correction is only on the order of several seconds. WASP-107b is one of the lowest density exoplanets known to date and thus has one of the highest bulk scale heights of any exoplanet, so it can be taken as an upper limit for what this overcompensation would be for any general exoplanet. The range of magnitudes of limb asymmetry in nature is not known, but for a modest case of  $N = 1$  or  $2$  this correction is generally less than one second.

## 4. DISCUSSION

### 4.1. *Implications for literature ephemerides*

The majority of, if not all, measurements of exoplanet transit times in the literature result from fitting data using a uniform-limb transit model. An immediate implication of this is that if any of these planets have limb asymmetry, these literature measurements are biased, particularly if they only used observations in a single bandpass. As we have shown, even for moderate limb asymmetry these literature times of conjunction may be biased by several to tens of seconds due purely to the planet's limb asymmetry, as well as an additional couple seconds of bias due to the numerical extra-area compensation effect. In all cases, we find that the physical bias in the time of conjunction due to limb asymmetry is larger than the numerical extra-area compensation effect. These biases are exaggerated for planets with high atmospheric scale heights, though this may actually work in their favor as, in these cases, it may be easier to measure the transit times with uncertainty smaller than the expected bias using multi-wavelength observations.



**Figure 8.** Magnitude of the numerical extra-area compensation effect as a function of limb radius difference, calculated for various representative exoplanets using Equation 18. This effect represents an additional bias in the measured time of conjunction of a planet with asymmetric limbs to what we derive in Equation 11 due to the goodness-of-fit metric optimization method used by numerical fitting techniques. For limb asymmetry of a few scale heights difference between limb radii, this compensation is on the order of one second. We find that planets with higher atmospheric scale heights have larger compensations for a given degree of limb asymmetry, as the slopes of the lines shown here increase in order of increasing scale height.

332

Our work here assumes having just a single light curve, such as a band-integrated observation, which underscores the potential danger in relying on a single-band observation for measuring a precise time

333

of conjunction if interested in investigating limb asymmetry. Other works in the literature have discussed the utility of instead using a multi-wavelength approach (e.g. Powell et al. 2019), where the different spectral variations of each limb’s radius compared to having a single, non-wavelength dependent time of conjunction reduces the strength of their degeneracy. Even if this physical bias is eliminated, however, fits of the time of conjunction may still be biased by the numerical extra-area compensation effect. Although this effect is relatively small, it will be relevant for very high-precision times, with uncertainties less than one second, that are currently possible with combined JWST observations (e.g. Murphy & et al. 2023b, in review; Carter & et al. 2023, in preparation). We recommend always considering all potential biases when using a literature transit time for an analysis of limb asymmetry.

#### 4.2. Additional effects on the observability of limb asymmetry

Some exoplanets exhibit transit timing variations (TTVs) induced by gravitational interaction with other planets in the same system (e.g. Maciejewski et al. 2010; Adams et al. 2011). The amplitude of these TTVs can range from less than one second to tens of minutes depending on the orbital architecture of the system, and have variation periods upwards of hundreds of years. For certain planets, these TTVs may place a limit on the achievable precision on a planet’s time of conjunction that is comparable or worse than the timing biases derived here. Therefore, unless the underlying TTV trend is known extremely well, it will likely be difficult to disentangle signatures of limb asymmetry from the uncertainty in the time of conjunction generated by TTV interactions for such planets.

Stellar surfaces are not perfectly homogeneous, and many exoplanet-hosting stars are known to have starspots and faculae on their surfaces. These stellar surface heterogeneities influence the signal observed during a planet’s transit, which can lead to biased inferences of the planet’s atmosphere if not properly accounted for (e.g. Rackham et al. 2018, 2019; Barclay et al. 2021; Moran et al. 2023). We did not consider the impact of stellar surface heterogeneities in this work and always assumed uniformly bright stellar disks. Our results apply most directly to scenarios when any stellar contamination can

360 be confidently ruled out or modeled. A more detailed study is warranted to examine how stellar  
361 contamination could further mimic or bias inferences of exoplanet limb asymmetry.

362 Finally, our analysis constructed the disk of an asymmetric-limb planet by explicitly assuming  
363 east-west asymmetry where each hemisphere is a uniform semi-circle. Real exoplanet atmospheres  
364 are likely not this ideal. For example, strong meridional circulation that preferentially transports  
365 condensates to a planet's polar regions may cause pole-equator asymmetry that is more significant  
366 than east-west asymmetry (e.g. see Parmentier et al. 2013; Charnay et al. 2015; Line & Parmentier  
367 2016). In this case, the planetary disk would be shaped differently than we have assumed, either as  
368 a 90-degree rotation or even a non-semi-circular shape, which would likely lead to a different form of  
369 the limb asymmetry - transit timing degeneracy than we have derived here.

## 370 5. SUMMARY

371 Measuring morning-to-evening variations of temperature, elemental and molecular abundances, and  
372 aerosol properties in exoplanet atmospheres is critical to understanding the underlying circulation  
373 and dynamics of the atmosphere. Transit observations are able to extract the separate contributions  
374 from a planet's morning and evening terminator using high-resolution ground-based spectroscopy  
375 and, more recently, low-resolution space-based spectroscopy with JWST. Particularly for the latter,  
376 a strong degeneracy exists between the effect of limb asymmetry on a light curve and uncertainty in  
377 the planet's time of conjunction. In this work, we have described the origin of this degeneracy and  
378 derived an analytical formula for it, given in Equation 11. We find that limb asymmetry of one to  
379 two scale heights difference in limb radii can cause upwards of ten seconds in bias to the measured  
380 time of conjunction. Further, we find that this bias is more extreme for planets with larger scale  
381 height. When comparing our analytical framework to simulated observations of an asymmetric-limb  
382 planet fit using a uniform-limb model, we find that there is an additional bias to the inferred time  
383 of conjunction due to the goodness-of-fit metric used by numerical techniques. We dub this the  
384 "extra-area compensation effect" as it stems from the relative occulting areas of a uniform-limb disk  
385 and asymmetric-limb disk when stacked atop one another, and derive an analytical formula for it as

386 well in Equation 18. This extra-area compensation effect can be of the order a couple seconds for  
 387 moderate limb asymmetries, and must also be considered when investigating limb asymmetry.

388 The authors would like to acknowledge Kevin Hardegree-Ullman, Megan Mansfield, and Everett  
 389 Schlawin for helpful discussions that inspired this study. M.M.M. acknowledges funding from  
 390 NASA Goddard Spaceflight Center via NASA contract NAS5-02105. This material is based upon  
 391 work supported by the National Aeronautics and Space Administration under Agreement No.  
 392 80NSSC21K0593 for the program “Alien Earths”. The results reported herein bene- fited from  
 393 collaborations and/or information exchange within NASA’s Nexus for Exoplanet System Science  
 394 (NExSS) research coordination network sponsored by NASA’s Science Mission Directorate.

395 *Facilities:* Exoplanet Archive

396 *Software:* batman (Kreidberg 2015), catwoman (Jones & Espinoza 2022; Espinoza & Jones 2021b),  
 397 emcee (Foreman-Mackey et al. 2013), matplotlib (Hunter 2007), NumPy (Harris et al. 2020), PandExo  
 398 (Batalha et al. 2017), SciPy (Virtanen et al. 2020)

## REFERENCES

- 399 Adams, E. R., López-Morales, M., Elliot, J. L.,  
 400 Seager, S., & Osip, D. J. 2011, ApJ, 728, 125,  
 401 doi: [10.1088/0004-637X/728/2/125](https://doi.org/10.1088/0004-637X/728/2/125)
- 402 Anderson, D. R., Collier Cameron, A., Delrez, L.,  
 403 et al. 2017, A&A, 604, A110,  
 404 doi: [10.1051/0004-6361/201730439](https://doi.org/10.1051/0004-6361/201730439)
- 405 Apai, D., Karalidi, T., Marley, M. S., et al. 2017,  
 406 Science, 357, 683, doi: [10.1126/science.aam9848](https://doi.org/10.1126/science.aam9848)
- 407 Barclay, T., Kostov, V. B., Colón, K. D., et al.  
 408 2021, AJ, 162, 300,  
 409 doi: [10.3847/1538-3881/ac2824](https://doi.org/10.3847/1538-3881/ac2824)
- 410 Batalha, N. E., Mandell, A., Pontoppidan, K.,  
 411 et al. 2017, PASP, 129, 064501,  
 412 doi: [10.1088/1538-3873/aa65b0](https://doi.org/10.1088/1538-3873/aa65b0)
- 413 Beatty, T. G., Marley, M. S., Gaudi, B. S., et al.  
 414 2019, AJ, 158, 166,  
 415 doi: [10.3847/1538-3881/ab33fc](https://doi.org/10.3847/1538-3881/ab33fc)
- 416 Bonomo, A. S., Desidera, S., Benatti, S., et al.  
 417 2017, A&A, 602, A107,  
 418 doi: [10.1051/0004-6361/201629882](https://doi.org/10.1051/0004-6361/201629882)
- 419 Borsa, F., Allart, R., Casasayas-Barris, N., et al.  
 420 2021, A&A, 645, A24,  
 421 doi: [10.1051/0004-6361/202039344](https://doi.org/10.1051/0004-6361/202039344)

- 422 Bourrier, V., Ehrenreich, D., Lendl, M., et al.  
 423 2020, A&A, 635, A205,  
 424 doi: [10.1051/0004-6361/201936640](https://doi.org/10.1051/0004-6361/201936640)
- 425 Buzenzi, E., Marley, M. S., Apai, D., & Lupu,  
 426 R. E. 2014, Cloud structure of brown dwarfs  
 427 from spectroscopic variability observations.  
 428 <https://arxiv.org/abs/1406.0210>
- 429 Caldas, A., Leconte, J., Selsis, F., et al. 2019,  
 430 A&A, 623, A161,  
 431 doi: [10.1051/0004-6361/201834384](https://doi.org/10.1051/0004-6361/201834384)
- 432 Carter, A.L., M. E., & et al. 2023, in preparation
- 433 Charnay, B., Meadows, V., Misra, A., Leconte, J.,  
 434 & Arney, G. 2015, ApJL, 813, L1,  
 435 doi: [10.1088/2041-8205/813/1/L1](https://doi.org/10.1088/2041-8205/813/1/L1)
- 436 Dai, F., & Winn, J. N. 2017, AJ, 153, 205,  
 437 doi: [10.3847/1538-3881/aa65d1](https://doi.org/10.3847/1538-3881/aa65d1)
- 438 Delisle, S., & et al. 2023, in preparation
- 439 Ehrenreich, D., Lovis, C., Allart, R., et al. 2020,  
 440 Nature, 580, 597,  
 441 doi: [10.1038/s41586-020-2107-1](https://doi.org/10.1038/s41586-020-2107-1)
- 442 Espinoza, N., & et al. 2023, in preparation
- 443 Espinoza, N., & Jones, K. 2021a, AJ, 162, 165,  
 444 doi: [10.3847/1538-3881/ac134d](https://doi.org/10.3847/1538-3881/ac134d)
- 445 —. 2021b, AJ, 162, 165,  
 446 doi: [10.3847/1538-3881/ac134d](https://doi.org/10.3847/1538-3881/ac134d)
- 447 Faedi, F., Barros, S. C. C., Anderson, D. R., et al.  
 448 2011, A&A, 531, A40,  
 449 doi: [10.1051/0004-6361/201116671](https://doi.org/10.1051/0004-6361/201116671)
- 450 Feinstein, A. D., Radica, M., Welbanks, L., et al.  
 451 2022, arXiv e-prints, arXiv:2211.10493,  
 452 doi: [10.48550/arXiv.2211.10493](https://doi.org/10.48550/arXiv.2211.10493)
- 453 Feng, Y. K., Line, M. R., Fortney, J. J., et al.  
 454 2016, ApJ, 829, 52,  
 455 doi: [10.3847/0004-637X/829/1/52](https://doi.org/10.3847/0004-637X/829/1/52)
- 456 Fischer, P. D., Knutson, H. A., Sing, D. K., et al.  
 457 2016, ApJ, 827, 19,  
 458 doi: [10.3847/0004-637X/827/1/19](https://doi.org/10.3847/0004-637X/827/1/19)
- 459 Foreman-Mackey, D., Hogg, D. W., Lang, D., &  
 460 Goodman, J. 2013, PASP, 125, 306,  
 461 doi: [10.1086/670067](https://doi.org/10.1086/670067)
- 462 Gaia Collaboration, Brown, A. G. A., Vallenari,  
 463 A., et al. 2018, A&A, 616, A1,  
 464 doi: [10.1051/0004-6361/201833051](https://doi.org/10.1051/0004-6361/201833051)
- 465 Harris, C. R., Millman, K. J., van der Walt, S. J.,  
 466 et al. 2020, Nature, 585, 357,  
 467 doi: [10.1038/s41586-020-2649-2](https://doi.org/10.1038/s41586-020-2649-2)
- 468 Hellier, C., Anderson, D. R., Collier Cameron, A.,  
 469 et al. 2014, MNRAS, 440, 1982,  
 470 doi: [10.1093/mnras/stu410](https://doi.org/10.1093/mnras/stu410)
- 471 Hoeijmakers, H. J., Cabot, S. H. C., Zhao, L.,  
 472 et al. 2020, A&A, 641, A120,  
 473 doi: [10.1051/0004-6361/202037437](https://doi.org/10.1051/0004-6361/202037437)
- 474 Hunter, J. D. 2007, Computing in Science &  
 475 Engineering, 9, 90, doi: [10.1109/MCSE.2007.55](https://doi.org/10.1109/MCSE.2007.55)
- 476 Jones, K., & Espinoza, N. 2022, Journal of Open  
 477 Source Software, 7, 2382,  
 478 doi: [10.21105/joss.02382](https://doi.org/10.21105/joss.02382)
- 479 Kataria, T., Sing, D. K., Lewis, N. K., et al. 2016,  
 480 ApJ, 821, 9, doi: [10.3847/0004-637X/821/1/9](https://doi.org/10.3847/0004-637X/821/1/9)
- 481 Kesseli, A. Y., & Snellen, I. A. G. 2021, ApJL,  
 482 908, L17, doi: [10.3847/2041-8213/abe047](https://doi.org/10.3847/2041-8213/abe047)
- 483 Kokori, A., Tsiaras, A., Edwards, B., et al. 2022,  
 484 ApJS, 258, 40, doi: [10.3847/1538-4365/ac3a10](https://doi.org/10.3847/1538-4365/ac3a10)

- 485 Kreidberg, L. 2015, PASP, 127, 1161,  
486 doi: [10.1086/683602](https://doi.org/10.1086/683602)
- 487 Line, M. R., & Parmentier, V. 2016, ApJ, 820, 78,  
488 doi: [10.3847/0004-637X/820/1/78](https://doi.org/10.3847/0004-637X/820/1/78)
- 489 Maciejewski, G., Dimitrov, D., Neuhäuser, R.,  
490 et al. 2010, MNRAS, 407, 2625,  
491 doi: [10.1111/j.1365-2966.2010.17099.x](https://doi.org/10.1111/j.1365-2966.2010.17099.x)
- 492 Maciejewski, G., Dimitrov, D., Mancini, L., et al.  
493 2016, AcA, 66, 55.  
<https://arxiv.org/abs/1603.03268>
- 494 Mancini, L., Esposito, M., Covino, E., et al. 2018,  
495 A&A, 613, A41,  
496 doi: [10.1051/0004-6361/201732234](https://doi.org/10.1051/0004-6361/201732234)
- 497 May, E. M., Stevenson, K. B., Bean, J. L., et al.  
498 2022, AJ, 163, 256,  
499 doi: [10.3847/1538-3881/ac6261](https://doi.org/10.3847/1538-3881/ac6261)
- 500 Metchev, S. A., Heinze, A., Apai, D., et al. 2015,  
501 The Astrophysical Journal, 799, 154,  
502 doi: [10.1088/0004-637x/799/2/154](https://doi.org/10.1088/0004-637x/799/2/154)
- 503 Moran, S. E., Stevenson, K. B., Sing, D. K., et al.  
504 2023, High Tide or Riptide on the Cosmic  
505 Shoreline? A Water-Rich Atmosphere or Stellar  
506 Contamination for the Warm Super-Earth  
507 GJ 486b from JWST Observations.  
<https://arxiv.org/abs/2305.00868>
- 508 Murphy, M., & et al. 2023b, in review
- 509 Parmentier, V., Showman, A. P., & Lian, Y. 2013,  
510 A&A, 558, A91,  
511 doi: [10.1051/0004-6361/201321132](https://doi.org/10.1051/0004-6361/201321132)
- 514 Patel, J. A., & Espinoza, N. 2022, AJ, 163, 228,  
515 doi: [10.3847/1538-3881/ac5f55](https://doi.org/10.3847/1538-3881/ac5f55)
- 516 Piaulet, C., Benneke, B., Rubenzahl, R. A., et al.  
517 2021, AJ, 161, 70,  
518 doi: [10.3847/1538-3881/abcd3c](https://doi.org/10.3847/1538-3881/abcd3c)
- 519 Powell, D., Louden, T., Kreidberg, L., et al. 2019,  
520 ApJ, 887, 170, doi: [10.3847/1538-4357/ab55d9](https://doi.org/10.3847/1538-4357/ab55d9)
- 521 Rackham, B. V., Apai, D., & Giampapa, M. S.  
522 2018, ApJ, 853, 122,  
523 doi: [10.3847/1538-4357/aaa08c](https://doi.org/10.3847/1538-4357/aaa08c)
- 524 —. 2019, AJ, 157, 96,  
525 doi: [10.3847/1538-3881/aaf892](https://doi.org/10.3847/1538-3881/aaf892)
- 526 Rustamkulov, Z., Sing, D. K., Mukherjee, S.,  
527 et al. 2022, arXiv e-prints, arXiv:2211.10487,  
528 doi: [10.48550/arXiv.2211.10487](https://doi.org/10.48550/arXiv.2211.10487)
- 529 Taylor, J., Parmentier, V., Irwin, P. G. J., et al.  
530 2020, MNRAS, 493, 4342,  
531 doi: [10.1093/mnras/staa552](https://doi.org/10.1093/mnras/staa552)
- 532 Triaud, A. H. M. J., Gillon, M., Ehrenreich, D.,  
533 et al. 2015, MNRAS, 450, 2279,  
534 doi: [10.1093/mnras/stv706](https://doi.org/10.1093/mnras/stv706)
- 535 Virtanen, P., Gommers, R., Oliphant, T. E., et al.  
536 2020, Nature Methods, 17, 261,  
537 doi: [10.1038/s41592-019-0686-2](https://doi.org/10.1038/s41592-019-0686-2)
- 538 von Paris, P., Gratier, P., Bordé, P., Leconte, J.,  
539 & Selsis, F. 2016, A&A, 589, A52,  
540 doi: [10.1051/0004-6361/201527894](https://doi.org/10.1051/0004-6361/201527894)